Structure and electrocatalytic performance of carbon-supported platinum nanoparticles☆

Isaac Esparbé, Enric Brillas, Francesc Centellas, José Antonio Garrido, Rosa María Rodríguez, Conchita Arias, Pere-Lluís Cabot*

Laboratori d'Electroquímica dels Materials i del Medi Ambient, Departament de Química Física, Facultat de Química, Universitat de Barcelona, Martí i Franquès 1-11, 08028 Barcelona, Spain

ABSTRACT

The structure of Pt nanoparticles and the composition of the catalyst-Nafion films strongly determine the performance of proton exchange membrane fuel cells. The effect of Nafion content in the catalyst ink, prepared with a commercially available carbon-supported Pt, in the kinetics of the hydrogen oxidation reaction (HOR), has been studied by the thin layer rotating disk electrode technique. The kinetic parameters have been related to the catalyst nanoparticles structure, characterized by X-ray diffraction and high-resolution transmission electron microscopy. The size-shape analysis is consistent with the presence of 3D cubo-octahedral Pt nanoparticles with average size of 2.5 nm. The electrochemically active surface area, determined by CO stripping, appears to depend on the composition of the deposited Pt/C-Nafion film, with a maximum value of $73 \, m^2 \, g_{Pt}^{-1}$ for 30 wt.% Nafion. The results of CO stripping indicate that the external Pt faces are mainly $(1\,0\,0)$ and $(1\,1\,1)$ terraces, thus confirming the cubo-octahedral structure of nanoparticles. Cyclic voltammetry combined with the RDE technique has been applied to study the kinetic parameters of HOR besides the ionomer resistance effect on the anode kinetic current at different ionomer contents. The kinetic parameters show that H_2 oxidation behaves reversibly with an estimated exchange current density of $0.27 \, mA \, cm^{-2}$.

© 2009 Elsevier B.V. All rights reserved.

1. Introduction

Proton exchange membrane fuel cells (PEMFCs) are efficient devices which can be satisfactorily used in transport applications [1]. The most extensively used catalysts for PEMFC are pure Pt and Pt alloys supported on carbons with high specific surface area. They are being improved by decreasing the particle size to 2–3 nm, increasing the particle dispersion and modulating the particle morphology [2–10].

Appropriate characterization techniques are needed to study the particle morphology, mainly X-ray diffraction (XRD) and high-resolution transmission electron microscopy (HRTEM) [11]. XRD reveals the lattice planes in the bulk structure, indicating the dominant crystallographic phase, and the 2D-projected HRTEM images show the size and symmetry of the nanoparticles. HRTEM is commonly used to determine the shape distribution, to analyse the effect of different synthesis methods and to relate morphology with

catalytic activity [12–15]. However, the usual procedure is counting the number of particles with a given shape, which is a hard-working manual task.

The catalysts can be electrochemically characterized on inert electrodes after suitable catalyst ink preparation and deposition [2,16,17]. The two-step deposition, consisting in covering with a Nafion thin film a previously deposited catalyst ink layer on an inert electrode, is frequently used to determine the kinetics of the hydrogen oxidation reaction (HOR), because hydrogen diffusion through the Nafion film is minimized when it is sufficiently thin [2,7,17].

A further step is to study the optimum ionomer content in the fuel cell membrane-electrode assembly (MEA) [18–22]. To build up the MEA, catalyst layers are extended on each side of the PEM (normally Nafion) from inks prepared with the catalyst and the membrane ionomer. The latter assures a sufficient extent of the three phase boundary in the electrode and helps to conduct the proton species generated during HOR between the electrode and the membrane. The optimum ionomer content is about 30–40 wt.% for Nafion and Flemion with carbon black supported catalysts. At Nafion percentages smaller than 30 wt.%, the poorer performance is explained by limited proton conductivity and incomplete wetting of catalyst by the ionomer [18,19]. When the ionomer content exceeds 40% the average pore diameter decreases, and the elec-

trode performance becomes diffusion-controlled [19–21]. It is also in agreement with E-TEK Pt/C Vulcan XC-72R 20 wt.% catalyst electrodes for the reduction of oxygen with an optimum 30% Nafion in the catalyst layer [23]. For E-TEK Pt/C Vulcan XC-72 20 wt.% catalyst electrodes in MEAs with 0.5, 0.25 and 0.1 mg cm^{-2} Pt loading, best performance was achieved at about 20, 40 and 50% Nafion ionomer loading, respectively, then showing a metal loading dependence [1].

In this work, a high performance (HP) E-Tek Pt-C catalyst is electrochemically characterized by one-step deposition of inks, made with the catalyst and different Nafion contents, on glassy carbon (GC) electrodes. This deposition procedure approaches the electrode preparation in real PEMFCs and allows studying the effect of the Nafion content on the catalyst layer performance. The electrochemically active surface area (ECSA) and the kinetics of HOR have been determined for such different electrode preparations using cyclic voltammetry (CV) and rotating disk electrode (RDE) technique, respectively. The structural characterization of the catalyst has been performed in parallel using XRD, TEM and HRTEM. Crystal structure, size, size distribution and homogeneity of the dispersion of the nanoparticles are thus obtained. The 3D morphology of the nanoparticles has been characterized by a novel method consisting in plotting the 2D area of the TEM section of the particles in front of their size, which allows the easy quantification of the different particle shapes compatible with their 3D structure. These plots also clarify the relation between particle morphology and catalytic activity in order to enhance the catalyst efficiency and reduce the catalyst amount in the fuel cell. E-Tek HP unsupported Pt has also been tested for comparison purposes.

2. Experimental

2.1. Reagents

The catalyst used in this work was E-Tek 20 wt.% HP Pt supported on carbon Vulcan XC-72 (actual analysis giving 19.6 wt.% Pt on carbon). Carbon Vulcan XC-72 and unsupported HP Pt powders were also obtained from E-Tek. The working electrodes were prepared from a catalyst dispersion (ink) obtained by sonicating 5–15 mg of carbon-supported Pt in a mixture of Millipore Milli-Q water (conductivity $<6 \times 10^{-8} \, \Omega^{-1} \, cm^{-1}$) with 5 wt.% solution of Nafion perfluorinated ion-exchange resin from Aldrich. Different proportions of water and Nafion solution were tested to check the effect of the quantity of Nafion with respect to the catalyst.

The electrolyte used for the electrochemical characterization and to study HOR was 0.5 mol dm^{-3} H$_2$SO$_4$, titrated with NaOH previously standardized with potassium hydrogen phthalate. These solutions were prepared with Millipore Milli-Q water, PRS NaOH from Panreac, analytical grade H$_2$SO$_4$ from Merck or analytical grade potassium hydrogen phthalate from Merck. The electrolyte was saturated with CO and Ar in the CO stripping experiments and with H$_2$ to study HOR. CO gas was Linde 3.0 (purity $\geq$99.9%), while Ar and H$_2$ gases were Linde 5.0 (purity $\geq$99.999%).

2.2. Structural characterization

The structural characterization of the samples was performed by means of XRD and TEM. X-ray diffraction patterns at angles (2θ) between 10 and 140° were recorded using a PANAlytical X'Pert PRO Alpha-1 diffractometer using Cu Kα radiation. The samples were supported on a Si-Xtal support. Diffraction patterns were modelled adjusting the experimental diffraction peaks to Pseudo–Voight equations using the WinPLOTR software in order to ascertain the crystallinity and determine the mean size of the particles.

The size distribution, dispersion homogeneity, crystallographic phases and morphology quantification of the particles were

obtained by TEM and HRTEM using a JEOL JEM 2010F TEM 200 KV with field emission gun. For such measurements, the samples were suspended in n-hexane with ultrasonic dispersion for 3 min. Then, a drop of this suspension was added to a holey carbon grid, which was ready for microscopic observation after drying. Electron energy loss spectroscopy (EELS) coupled to TEM was used to confirm the presence of the Pt nanoparticles and the absence of other metals. Images were recorded with a Gatan MultiScan 794 CCD camera. Particle crystalline phases were analysed with Fast Fourier Transform from images using a Gatan Digital Micrograph 3.7.0 software. CaRIne Cristallography 3.1 and PCpdfWin software's were used for the crystallographic identification.

2.3. Electrochemical measurements

The electrochemical experiments were performed in a conventional thermostated three-electrode Metrohm cell of 150 cm^3 capacity. The reference electrode was a double junction Ag|AgCl|Cl$^-$ (1.0 mol dm^{-3} KCl) electrode (E° = 0.236 V vs. reversible hydrogen electrode (RHE)) and the auxiliary electrode was a Pt rod. All the potentials given in this work are referred to the RHE. The working electrode was prepared on the clean surface of the GC tips of an Eco chemie Autolab RDE. GC tips with active surface diameters of 3 and 5 mm were employed. The motor speed was manually controlled in the range 800–2400 rpm. The electrolyte temperature was set at 25.0 $\pm$ 0.1 °C by water circulation through the double wall of the cell using a Julabo MP-5 thermostat.

The working electrodes were prepared just before the electrochemical measurements. The GC tip was polished up to mirror finish on a PSA-backed White Felt polishing cloth with aluminium oxide from Buehler with aqueous alumina suspensions of decreasing particle size up to 0.05 μm, cleaning in ultrasonic bath between polishing steps. Such suspensions were prepared by sonication with Millipore Milli-Q water and deagglomerated 0.3 μm α-alumina or 0.05 μm γ-alumina Micropolish II, also from Buehler. Cyclic voltammograms for GC after polishing allowed testing the surface finishing performance.

On the clean GC surface, a given volume of the carbon-supported Pt catalyst suspension in the range 1–3 μl was added, measured with a digital pipettor (Labopette Variabel from Hirschmann or Witopet from Witeg), and its weight was carefully measured with an accuracy of ±0.01 mg. Afterwards, the electrode was dried overnight at room temperature in a clean and dry atmosphere. The mass ratio of catalyst and ionomer was varied to find out the optimal composition for good attachment of the carbon support and good dispersion of the catalytic particles in order to obtain a suitable electric contact together with the optimal electroactive area. The catalyst concentration in the ink allowed obtaining final surface concentrations in the range 5–100 μg$_{Pt}$ cm^{-2}, typical values used previously for characterizing electroactive areas of Pt electrodes [24,25]. To prove the homogeneous distribution of the catalyst over the GC, Pt analyses in different regions on the electrode were performed using X-Ray Fluorescence (XRF) Spectroscopy (Fischer Fischerscope X-Ray System XDAL spectrometer), at 50 kV. Considering that it was difficult to cover exactly the section of the GC by the catalyst ink and that the real section of the latter is an important quantity to obtain kinetic parameters from the Koutecky–Levich plots, we used the images obtained by means of the video camera coupled to the XRF spectrometer together with the DigitalMicrograph software to determine the GC coverage by the catalyst ink (this was done after the electrochemical experiments to avoid contamination).

Cyclic voltammograms at scan rates in the range 10–100 mV s^{-1} starting at 0.03 V and reversing the sweep at different anodic limits were obtained for each prepared working electrode using a Solartron SI 1287 electrochemical interface commanded

by the Electrochemical/Corrosion CorrWare for Windows 2.6b software.

The ECSAs of the prepared electrocatalyst samples were determined by measuring the coulombic charge consumed for CO stripping and also for atomic hydrogen adsorption/desorption of underpotentially deposited hydrogen, treating the cyclic voltammograms with the help of a Solartron Analytical CView 2.6b program. To assure working with clean surfaces, the electrode potential was cycled several times between 0.03 and 1.00 V in Ar atmosphere. For CO stripping, pure CO was bubbled for 15 min through the electrolyte keeping the electrode potential at 0.1 V. Afterwards, Ar was bubbled through the electrolyte for 45 min to remove non-adsorbed CO and two consecutive cyclic voltammograms at 20 mV s^{-1} between 0.03 and 1.00 V were recorded.

To study HOR, single cyclic RDE voltammograms were consecutively obtained between 0.00 and 0.40 V vs. RHE for different rotation rates up to 2400 rpm at 5 mV s^{-1} after previous saturation of the electrolyte with H$_2$ by bubbling pure gas through the electrolyte for 60 min. The gas flow was kept over the electrolyte during the experiments. The ECSAs were also measured from the corresponding atomic hydrogen desorption peaks. A final CO stripping was performed to confirm the absence of significant catalyst loss from the electrode during consecutive RDE experiments.

3. Results and discussion

3.1. XRD analyses

The diffraction patterns of the carbon-supported and unsupported Pt catalysts are depicted in Fig. 1a and b, respectively. They contained a number of diffraction peaks that are consistent with the presence of Pt face centred cubic (FCC) phases, also indicated in such figures. The peak at 2θ equal to about 25° in Fig. 1a corresponds to carbon Vulcan XC-72.

The XRD pattern was divided into several groups of close peaks in order to mathematically model each part of the diffractogram individually to a single Pseudo–Voight equation. From this model, the angle (θ) and width (β) of each diffraction peak corresponding to each crystalline phase of the samples were obtained. The single crystal size (D_{hkl}) from each peak of Miller index (hkl) was then calculated by replacing these parameters in the Scherrer equation [26]:

$$D_{hkl} = \frac{\lambda}{\beta \cos\theta} \tag{1}$$

where λ is the length of Cu Kα incident radiation (1.5406 Å). The resulting average values using the above Scherrer's model were 2.5 ± 0.2 and 4.2 ± 0.5 nm for the supported and the unsupported Pt catalysts, respectively.

The crystallite size corrected for the particle shape anisotropy and micro-structural tension was also determined by applying the Williamson–Hall (W–H) model [27] using the following equations:

$$\beta^* = \frac{1}{D_v} + 2\varepsilon Q \tag{2}$$

$$Q = \frac{2\sin\theta}{\lambda} \tag{3}$$

where β^* is the integral width of a reciprocal lattice point ($=D_{hkl}^{-1}$), D_v is the mean apparent volume-weighted crystallite size, ε is the internal particle strain and Q is the distance of the point from the origin of the reciprocal lattice. Fig. 2 illustrates the β^*–Q plots for the HP 20 wt.% Pt/C Vulcan XC-72. The particle size was then determined from the inverse of the intercept at $Q=0$ of the above W–H plots. The crystallite sizes thus obtained were 2.6 ± 0.3 and 5.4 ± 0.8 nm for the supported and the unsupported Pt catalysts,
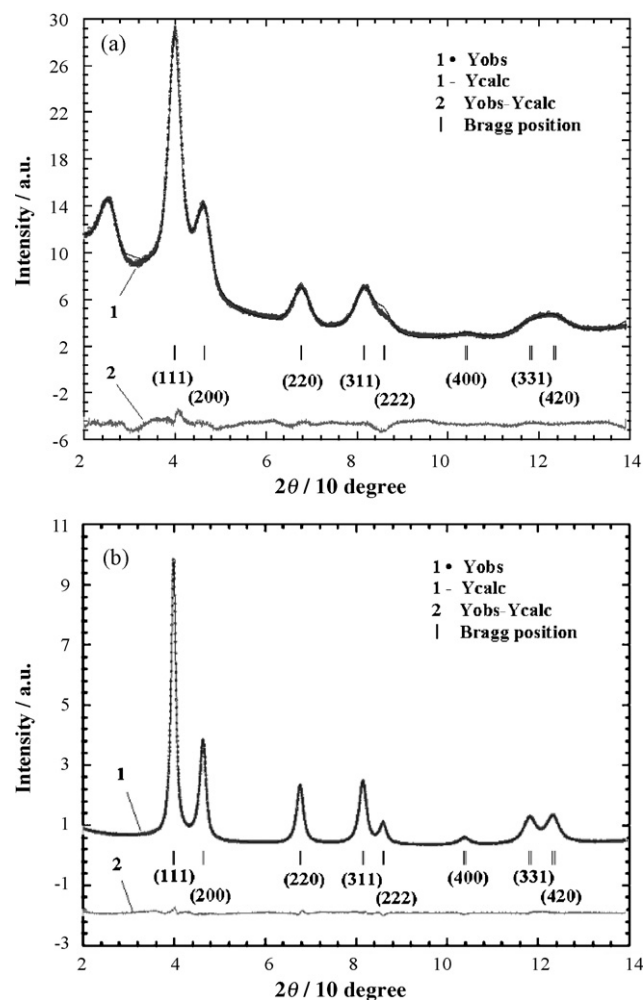

Fig. 1. XRD fitted patterns for (a) HP 20 wt.% Pt/C Vulcan XC-72 and (b) HP unsupported Pt catalyst. The Pt fcc markers are shown together with fitting (Y_{calc}) and the experimental points (Y_{obs}) in curve 1. Curve 2 shows the difference between the experimental curve and fitting.
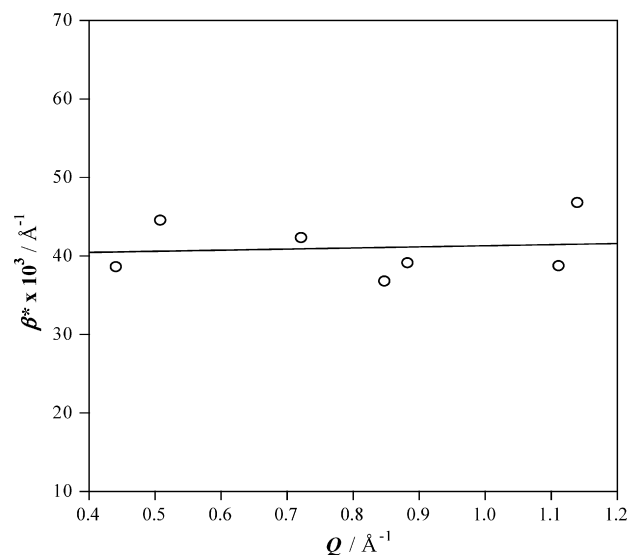

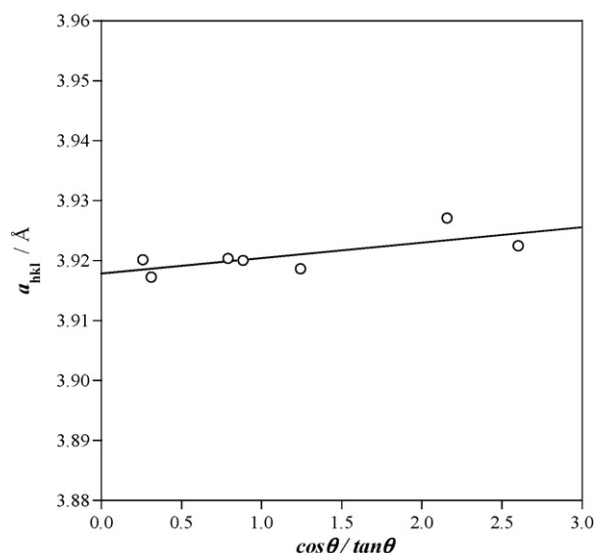**Fig. 2.** Williamson–Hall plot of XRD patterns for the HP 20 wt.% Pt/C Vulcan XC-72.

Fig. 3. Lattice constant position shifting plot for the HP unsupported Pt catalyst.

Fig. 4. TEM image of HP 20 wt.% Pt/C Vulcan XC-72.

respectively. These corrected average particle sizes calculated from W–H model correcting anisotropic and strain effects are slightly higher than those found from Scherrer equation stated above.

Assuming that particles are homogeneous and non-agglomerated with spherical form, the surface area (SA_{XRD}) can be calculated by Eq. (4):

$$SA_{XRD} = \frac{3}{r\rho_{cat}} \qquad (4)$$

where r is the particle radius and ρ_{cat} is the bulk density of the catalyst. From Eq. (4), surface areas of 107.5 and 51.8 m^2 g^{-1} for the corresponding supported and the unsupported catalysts were found. These data evidence that the carbon support favors the dispersion of the catalyst and the particle size is then smaller.

An initial value of the lattice constant (a) was obtained from every Pt plane by combining a FCC unit cell lattice parameter equation with Bragg's law:

$$\lambda = 2d \sin\theta \qquad (5)$$

where d is the spacing between the lattice planes. The effect of the peak position shifting caused by a variation of the sample position in the Z-axis due to transparency and gradation of the sample was corrected using Eq. (6):

$$a = a_0 - \left[\frac{a_0 \Delta Z \cos\theta}{R \tan\theta}\right] \qquad (6)$$

where a_0 is the corrected lattice constant, ΔZ is the position shifting and R is the diffractometer radius (240 nm). As an example, Fig. 3 shows the plot of a vs. [$\cos\theta/\tan\theta$] for the HP unsupported Pt catalyst. From such plots, values of 3.921 ± 0.004 and 3.918 ± 0.002 Å were determined for the corrected lattice constant of the supported and the unsupported Pt catalysts, respectively. These values are in very good agreement with those reported for bulk Pt lattice constant [28], corroborating that nanoparticles are mostly composed of nanocrystalline pure platinum.

3.2. TEM and HRTEM analyses

The low-magnification TEM images of the carbon-supported Pt catalyst showed a fine dispersion of Pt nanoparticles on carbon spheres, as can be seen in Fig. 4. EELS analyses of different parts of the sample confirmed the identification of the Pt nanoparticles together 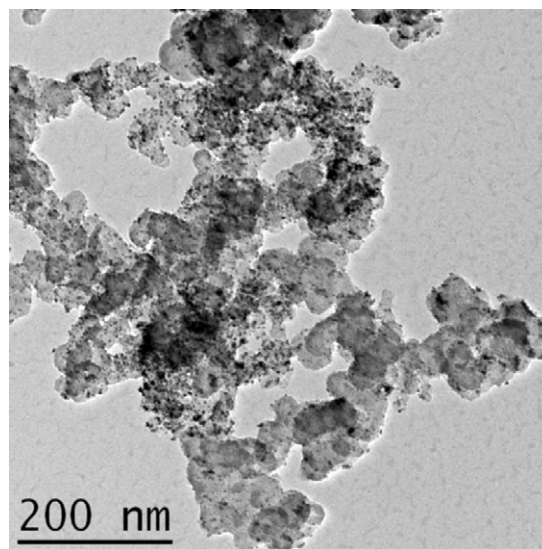with their form and dispersion. A further magnification is shown in Fig. 5, which also shows the structure of Carbon Vulcan XC-72. To try to do an approach with respect to the homogeneity of the distribution of the nanoparticles in the carbon spheres, in the absence of other quantitative proposals in the literature, the same method as that used to study tracer particles dispersion in an internally circulating fluidised bed, based on the analysis of the inhomogeneity of particle flow in square grids, has been considered [29]. In this method, a free-sized square region containing about 50 particles and a grid with 3×3 square cells has to be depicted and then, the inhomogeneity factor given by the ratio SD/N_{cell}, where N_{cell} is the average number of particles per grid cell and SD its standard deviation with respect to all the cells of the image, is calculated. As the minimum inhomogeneity is zero ($SD = 0$), which corresponds to a maximum homogeneity, we propose a homogeneity factor as

$$H = \left(1 - \frac{SD}{N_{cell}}\right) \times 100 \qquad (7)$$

with a maximum value of 100%. In the picture of Fig. 5a, H is equal to 59% (note that a comparable H-value of 57% is obtained when the quantity of cells is 16, Fig. 5b). When calculating the H-values for the distribution of Pt nanoparticles supported on mesoporous carbon obtained in our laboratories [9,30], not previously reported, greater H-values between 81 and 87% have been obtained, indicating more homogeneous distributions. The homogeneity factor and the preliminary results obtained here open the way for a quantitative measurement of the homogeneity of the samples. Further work is being planned to develop such a quantitative procedure, which we consider that it is now out of the scope of the present paper.

To quantify the particle size and 2D shape at the same time, the area of the 2D TEM projections of the particles were plotted vs. their particle size. Firstly, TEM images were filtered in order to improve the contrast and a number of single particles greater than one-hundred were selected by using a contrast histogram plot. The area and size of each selected particle were further automatically calculated using the image size calibration factor and finally, the area of each particle was represented vs. its size. Fig. 6 presents the shape-size plot thus obtained for the sample of HP 20 wt.% Pt/C Vulcan XC-72. Note that nanoparticles were distinguished as circular, square and hexagonal 2D shapes in the microscope. To quantify the relative proportion of these forms, their theoretical geometric area was then determined as a function of their length (also shown in Fig. 6) and the 2D shape of each nanoparticle was assigned from comparison of the y/x^2
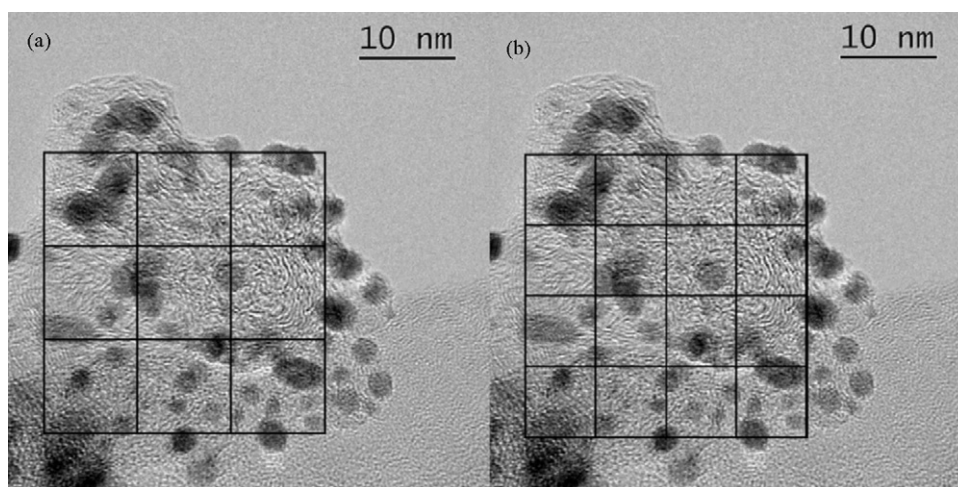
Fig. 5. TEM image of HP 20 wt.% Pt/C Vulcan XC-72 to calculate the *H* factor using (a) 3 × 3 and (b) 4 × 4 cells in a grid of about 50 nanoparticles.

factor of each theoretical shape curve with that experimentally obtained. As a result of this analysis, the 2D morphological profile of Fig. 6 agrees with 73% hexagonal-, 24% square- and 3% circular-shaped particles. These percentages of 2D shape projections are consistent with a dominant 3D cubo-octahedral particle morphology of the Pt nanoparticles in the carbon-supported catalyst.

From the percentage of frequency vs. particle size determined from the above analysis (see, for example, the inset of Fig. 6), an average particle size of 2.4 ± 0.6 nm for the supported Pt catalyst and 4.4 ± 0.8 nm for the unsupported Pt catalyst was found. These results are in agreement with those obtained by XRD. Note, however, that XRD values correspond to a much greater amount of particles, since a much higher amount of specimen is involved in the measurements.

The structural study of individual Pt nanoparticles by using FFT of HRTEM images is shown in Fig. 7. Typical Pt (1 1 1) and Pt (1 0 0) planes with a crystalline phase assignation error smaller than 3%

can be observed. The carbon Vulcan crystalline planes analysed in the same manner differed from conventional graphitic carbon.

3.3. ECSA of the catalyst

An example of the images obtained from the XRF spectrometer facilities is shown in Fig. 8, where the analyses of different regions of the electrode surface are also shown. In this case, the Pt content was 3.06 ± 0.03 wt.%, proving a good homogeneity of the catalyst ink over the GC. However, this has not to be considered the true Pt content in the catalyst ink, since some penetration by the X-rays into the GC support is expected. On the other hand, the section of the GC surface covered by the catalyst ink in this case was of 88%.

A base cyclic voltammogram showing the hydrogen adsorption/desorption region between 0.03 and 0.40 V [2,3,7] is depicted in Fig. 9a. Previous work allows deducing that the peak at 0.12 V should correspond to low-coordination Pt edge and corner atoms (Pt (1 1 0) sites vicinal to Pt (1 1 1)), and the following ones, up to 0.40 V, to Pt (1 0 0) terrace vicinal to Pt (1 1 1) sites. In addition, the wide peak at about 0.5 V could be due to the presence of the typical Pt (1 1 1) terrace sites of the cubo-octahedral nanoparticles [3], although it is also the same potential region were sulphate is adsorbed [31–33]. Peaks at about 0.9 V correspond to Pt oxidation. It
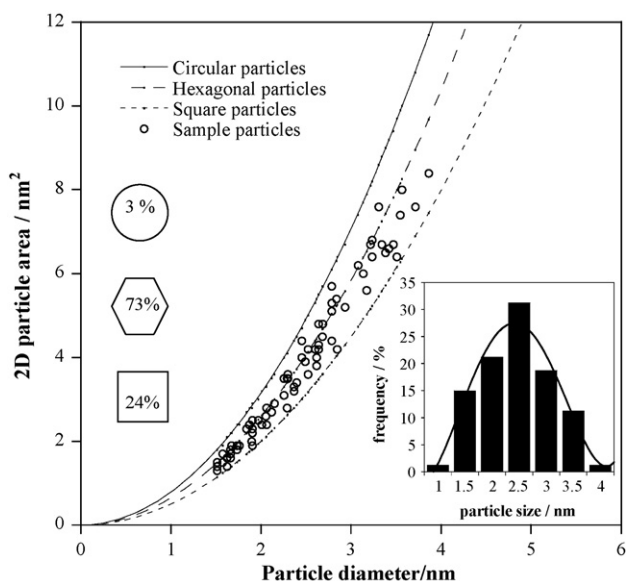

Fig. 6. Shape-size plot for the nanoparticles of HP 20 wt.% Pt/C Vulcan XC-72 sample. Theoretical curves assuming circular, hexagonal and square nanoparticle shapes calculated from the corresponding geometric area are specified. The morphological quantification and the particle size distribution for 103 particles are shown in the insets.
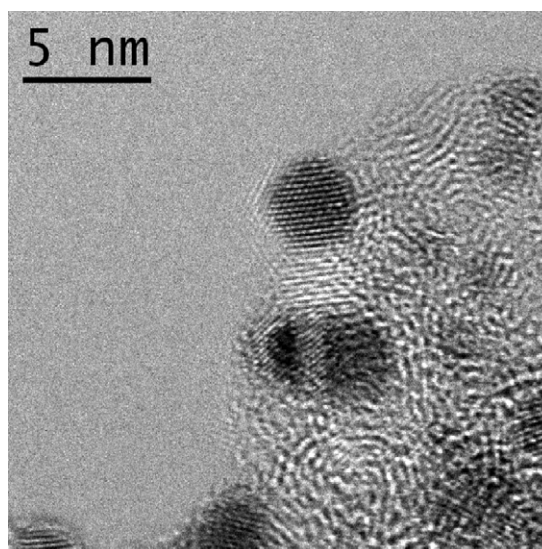

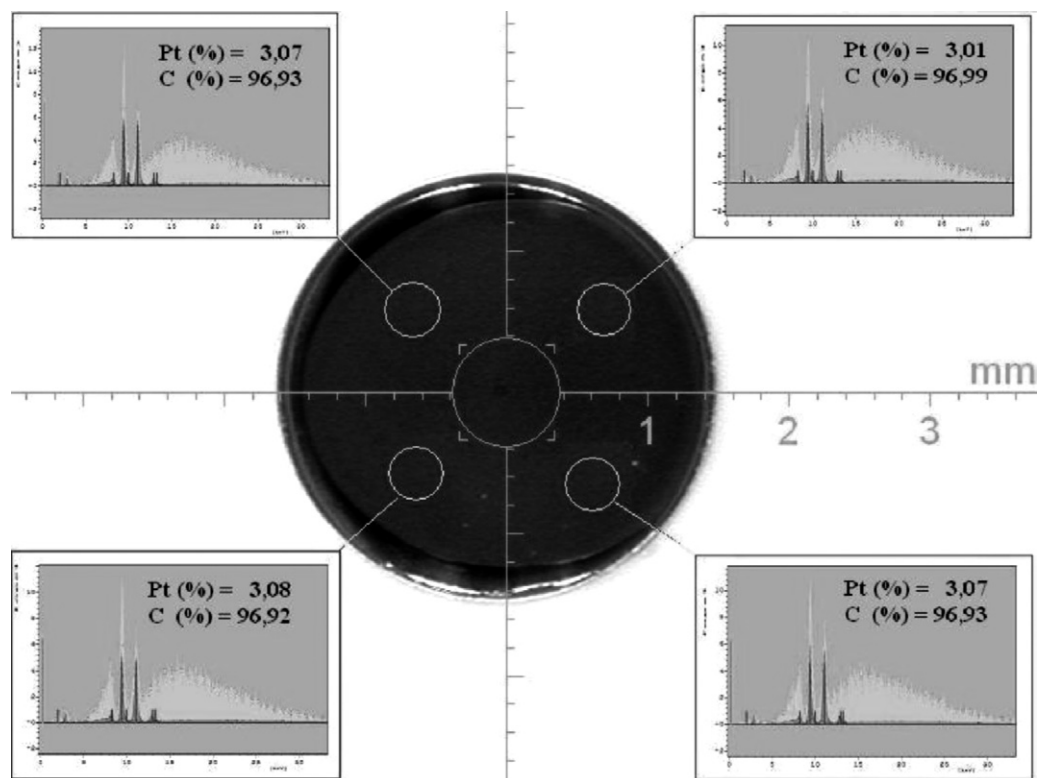**Fig. 7.** High-resolution TEM image of Pt nanoparticles on carbon Vulcan XC-72.

Fig. 8. XRF video camera image of a catalyst layer on the GC with a metal loading of 88.7 μg_{Pt} cm^{-2} and a Nafion content of 32.1 wt.% including XRF spectrum expressing Pt/C composition for the 4 different regions analysed.

is quite surprising that the peak at 0.5 V is very small compared with those in the range 0.03–0.40 V, because the cubo-octahedral particles mainly consist of external Pt (1 1 1) and Pt (1 0 0) terrace sites, the former being dominant by about 65% [7] (the ratio between the (1 1 1) and (1 0 0) surface atoms in the regular cubo-octahedron reported in [15] is 0.67). Further insight on this peak is discussed from the CO stripping voltammograms detailed below.

As shown in Fig. 9b, the CO stripping voltammograms essentially show a peak at about 0.8 V, which can be assigned to the contribution of Pt (1 0 0) and Pt (1 1 1) terrace sites [7]. The CO stripping peak on Pt (1 1 0) terraces should appear at about 0.7 V, which it is essentially missing in Fig. 9b and, therefore, CO stripping curves are consistent with the cubo-octahedral form of the Pt nanoparticles shown by XRD and TEM. Note also that the current of the anodic peak at 0.5 V in the post CO stripping voltammogram is only slightly greater than the current of the CO stripping curve, suggesting that hydrogen adsorption/desorption on Pt (1 1 1) terraces does not contribute significantly to the cyclic voltammetric behavior of Fig. 9a and b. Further evidence about this can be found when determining the ECSAs from CO stripping and from hydrogen adsorption/desorption. When the CO stripping was considered, the charge of the post CO stripping voltammogram was subtracted from the first stripping charge in the potential region of CO electro-oxidation (see Fig. 9b) considering a charge of 420 μC cm^{-2} for CO oxidation on polycrystalline Pt [34]. The dependence of ECSA on Nafion content in the catalyst ink is shown in Fig. 10. The maximum value of about 30 wt.% of the ionomer is in very good agreement with the optimal Nafion or Flemion contents of 30–40 wt.% in fuel cell MEAs [18–22,35] and therefore, the same explanation for the maximum in Fig. 10 can be given. At low Nafion percentages, the smaller ECSA can be explained by limited proton conductivity and incomplete wetting of the catalyst by the ionomer, which decreases the ECSA [18,19], whereas at high ionomer content, the electrode performance appears to be diffusion controlled [19–22].

After finding the most suitable Nafion content in the catalyst layer, different amounts of the catalyst were extended on the GC by varying the amount of water in the ink preparation in order to find a mean ECSA value. The corresponding results are presented in Fig. 11. As shown in curve (*a*), the mean ECSA value obtained from CO stripping was 73 m$_{Pt}^2$ g$_{Pt}^{-1}$. This parameter was also determined from the hydrogen adsorption/desorption peak charges in the range 0.03–0.40 V after subtracting the double layer charge contribution [2,7], assuming a charge of 210 μC cm^{-2} for hydrogen adsorption/desorption on polycrystalline Pt [36]. As can be seen in curve (*b*) of Fig. 11, a mean value of 69 m$_{Pt}^2$ g$_{Pt}^{-1}$ is found in this case, comparable to that obtained from CO stripping. It has to be noted that practically the same mean ECSA value was determined from both hydrogen adsorption and hydrogen desorption. Apart from that the ECSA value found from CO stripping is probably more precise because the peak charges are greater, the similar values obtained from both procedures indicate that essentially all the hydrogen is adsorbed and desorbed in the potential range between 0.03 and 0.40 V. To explain the absence of significant contribution of hydrogen desorption in the anodic sweep at potentials around 0.5 V we suggest that adsorbed hydrogen spills by surface diffusion from Pt (1 1 1) sites to (1 1 0) and (1 0 0) ones, thus increasing the hydrogen desorption peaks in the range 0.03–0.40 V. Then, only sulphate would be mainly adsorbed at potentials around 0.5 V. In the cathodic sweep, adsorbed sulphate could preclude hydrogen adsorption at these potentials and after sulphate desorption, hydrogen could start adsorbing at more negative potentials, spilling over the (1 1 1) sites. A similar spillover phenomenon has been previously invoked to justify the increase in the hydrogen oxidation rate through hydrogen diffusion anodes based on Pd foils covered by a thin film of Pt black [37]. This could explain why adsorption/desorption on Pt (1 1 1) terraces at 0.5 V is essentially featureless.
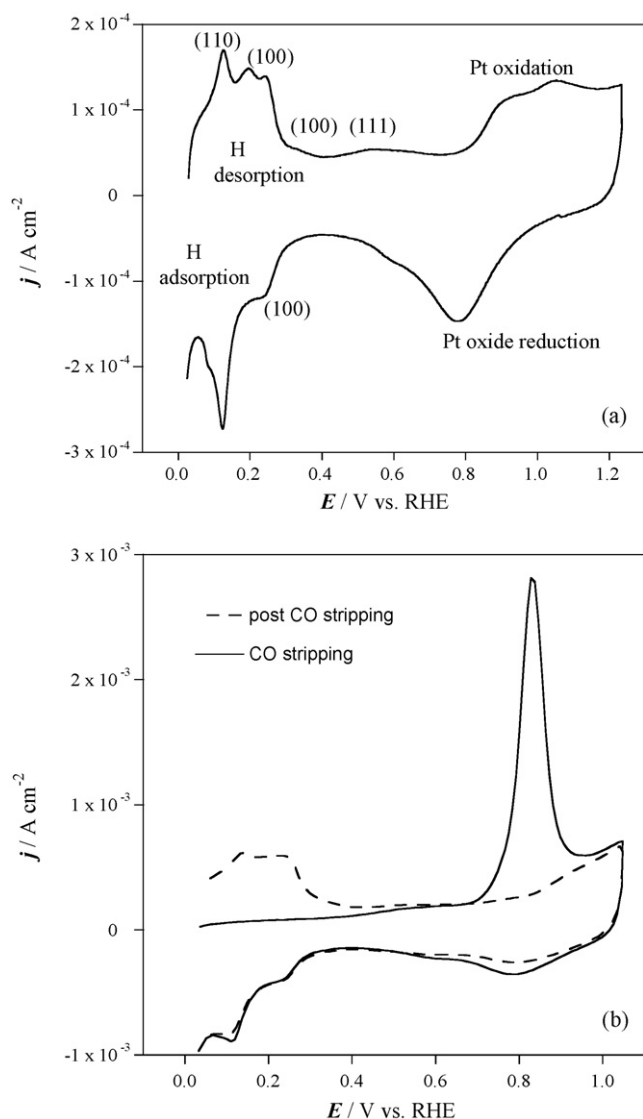
Fig. 10. CO oxidation ECSA vs. percentage of ionomer in the catalyst ink. Pt charge 37.5 μg_{Pt} cm^{-2}.

trode section (j_L), corrected by the real electrode coverage by the catalyst ink, for each rotation speed. Fig. 12 depicts the anodic curve of the linear sweep voltammograms recorded for HP 20 wt.% Pt/C Vulcan XC-72 deposited with 28.5 wt.% Nafion on GC between 800 and 2400 rpm at 5 mV s^{-1}. Assuming that the one-step deposition leads to a catalytic film structure similar to that obtained from the two-step deposition, i.e. the hydrogen molecules are transported from the electrolyte to the inner part of the film where they are oxidized, crossing some Nafion film thickness, the inverse of the limiting current density can be written as follows [39]:

$$\frac{1}{j_L} = \frac{1}{j_d} + \frac{1}{j_k} + \frac{1}{j_f} \tag{8}$$

where j_d is the current density limited by the H$_2$ diffusion through the electrochemical double layer, j_k is the kinetic current density

Fig. 9. Cyclic voltammograms for HP 20 wt.% Pt/C Vulcan XC-72 deposited with Nafion on GC for (a) atomic hydrogen adsorption/desorption, Pt charge of 8.5 μg_{Pt} cm^{-2} and (b) CO stripping and post CO stripping, Pt charge 37.5 μg_{Pt} cm^{-2}. Scan rate 20 mV s^{-1}. The amount of Nafion in the catalyst layer on the GC was 30 wt.%.

Note in addition that the surface area for the supported catalyst, calculated from XRD from the spherical approach, is 108 m_{Pt}^2 g_{Pt}^{-1}, which is higher than that obtained from CO stripping. This suggests that not all the surface area of the particles is available for CO oxidation, possibly due to the agglomeration of particles and shape anisotropy. However, it has also to be taken into account that the real CO-Pt stoichiometry is under discussion and that it is quite agreed that it is far from one. This could explain, at least partially, the discrepancy between the values as determined from stripping or XRD calculations. The high ECSA values obtained for the supported Pt catalyst studied in this work, when compared with 51 m_{Pt}^2 g_{Pt}^{-1} reported for the non HP carbon-supported Pt catalyst [38], make in evidence that it is an interesting material to be used as reference material in the catalyst development for PEMFCs.

3.4. Kinetics of the HOR on the Pt/C catalyst

The effect of Nafion content in the catalytic film on the kinetics of HOR has been studied obtaining the RDE voltammetric curves and measuring the limiting current density referred to the GC elec-
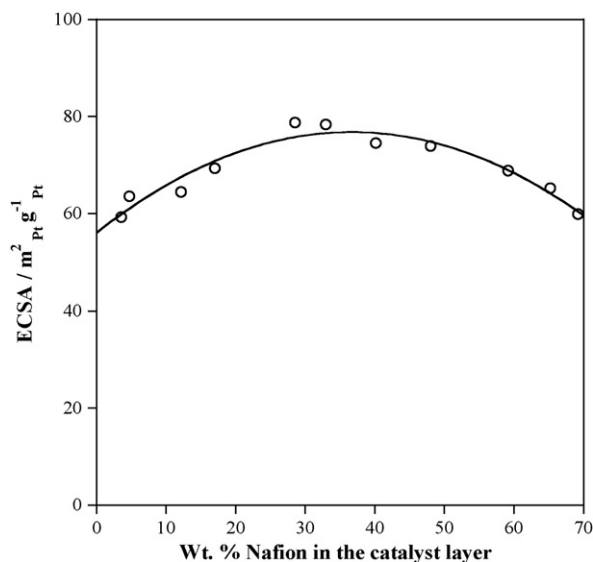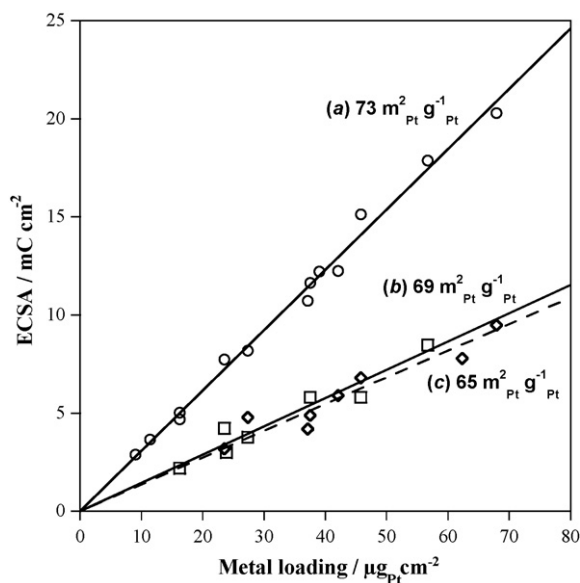

Fig. 11. Electrochemical active surface areas of Pt vs. metal loading for HP 20 wt.% Pt/C Vulcan XC-72 deposited with Nafion on GC determined from: (a) CO stripping, (b) atomic hydrogen adsorption/desorption after CO stripping and (c) atomic hydrogen desorption in the H$_2$ oxidation experiments. In (a) and (b) the amount of Nafion in the catalyst layer on GC was 30 wt.%.
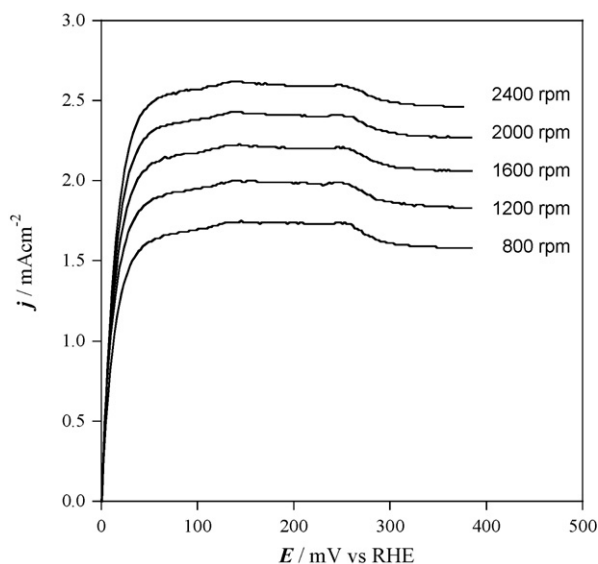
Fig. 12. Anodic curve of linear sweep RDE voltammograms obtained for HOR on HP 20 wt.% Pt/C Vulcan XC-72 deposited with 28.5 wt.% Nafion on GC at rotation speeds in the range 800–2400 rpm. Pt charge 45.8 μg_{Pt} cm^{-2}. Scan rate 5 mV s^{-1}.

and j_f is the current density limited by H$_2$ diffusion into Nafion. The former is given by:

$$j_d = B\,C_o\,\omega^{1/2} \qquad (9)$$

where C_o is the solubility of H$_2$ in the electrolyte, ω is the rotation speed and B is the Levich constant:

$$B = 0.62\,nF\,D^{2/3}\nu^{-1/6} \qquad (10)$$

In Eq. (10), n is the number of electrons involved in the oxidation reaction of H$_2$ (=2), F is the Faraday constant (96,487 C mol^{-1}) and D is the diffusion coefficient of H$_2$ in the electrolyte of viscosity ν. Plotting the inverse of j_L in front of $\omega^{-1/2}$ the so-called Koutecky–Levich diagram is obtained, in which the slope is equal to $(BC_o)^{-1}$ and $(1/j_k + 1/j_f)$ can be calculated by extrapolation. The BC_o value determined in this form was $(6.5 \pm 0.5) \times 10^{-2}$ mA cm^{-2}, close to the expected theoretical value of 6.54×10^{-2} mA cm^{-2} for HOR [7], confirming that the electrode area is the GC section. Fig. 13 presents the curve obtained by plotting the inverse of the Levich intercept $(1/j_k + 1/j_f)^{-1}$ vs. the inverse of the Nafion content. It appears to
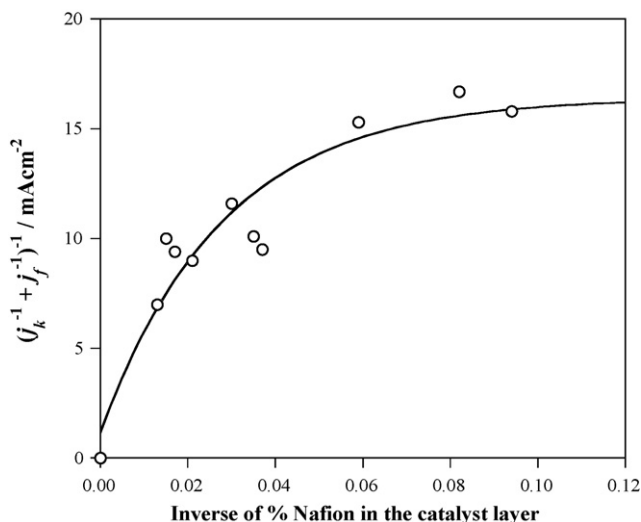

Fig. 13. Inverse of the Levich intercept with respect to the inverse of Nafion percentage in the catalyst layer deposited in one step on the GC.

asymptotically rise to a constant value, similar to that found when the thin-film electrodes were prepared by means of a two-step deposition [7]. This suggests that for one-step deposition, a Nafion film covers the Pt-catalyzed carbon spheres for sufficiently high ionomer content. However, other contributing factors can affect the shape of curve shown in Fig. 13. For example, when mixing Nafion with the carbon spheres, the latter components are expected to be separated by Nafion molecules and hence, their mean distance decreases as less Nafion is added. This would correspond to a higher Pt concentration in a given section of the thin-film electrode, favoring HOR with the subsequent increase in limiting current density.

It is well known that j_f is inversely proportional to the Nafion thickness in the two-step deposition [7,17] and also for Nafion films covering rotating disk Pt electrodes [5]. It could also be expected a similar variation of this parameter for the catalytic film prepared by one-step deposition. Thus $(1/j_k + 1/j_f)$ will approach $1/j_k$ for sufficiently thin films and small Nafion contents, the kinetic current becoming then the limiting factor. Accordingly, the change of $(1/j_k + 1/j_f)^{-1}$ with the inverse of the Nafion content will asymptotically approach j_k for sufficiently small Nafion contents. The trend depicted in Fig. 13 confirms this behavior, showing that the kinetic current density approaches 15 mA cm^{-2} when the ionomer content is smaller than about 20 wt.%. This j_k value is smaller than 40 mA cm^{-2} reported when the electrodes were prepared by two-step deposition [7]. However, it has to be taken into account that the kinetic current density depends on the amount of Pt present at the electrode film section were H$_2$ is effectively oxidized. In the present work, the Pt-catalyzed carbon spheres are expected to be mixed with Nafion molecules and therefore, the Pt concentration at a given film section is smaller than in the absence of the ionomer.

On the other hand, ECSA values were also obtained from the hydrogen desorption peaks of the hydrodynamic j–E curves for H$_2$ oxidation shown in Fig. 12, after extrapolating to zero the GC electrode rotation speed. A mean value of 65 ± 6 m$^2_{Pt}$ g$^{-1}_{Pt}$ is found (see curve (c) of Fig. 11), indicating that the catalytic film on the GC RDE was strongly attached. This was also confirmed by final CO stripping experiments.

To clarify the reversibility of HOR, the initial anodic current density growth of the RDE polarization data of Fig. 12 was analysed in terms of mass transport corrected Tafel diagrams. Under these conditions, the corresponding theoretical equations for reversible and irreversible electrochemical reactions can be written as Eqs. (11) and (12), respectively [8,38].

$$E = E_1^0 - \left(\frac{2.303\,RT}{nF}\right) \log\left[\frac{j_L - j}{j_L}\right] \qquad (11)$$

$$E = E_2^0 + \left(\frac{2.303\,RT}{0.5\,nF}\right) \log\left[\frac{j}{j_L - j}\right] \qquad (12)$$

where E_1^0 and E_2^0 are constant potential values for a given j_L and n is equal to 2. To discriminate between both possibilities, the plots of $\log[(j_L - j)/j_L]$ or of $\log[j/(j_L - j)]$ in front of E should be linear if Eqs. (11) or (12) is verified. The corresponding Tafel plots obtained for HP 20 wt.% Pt/C Vulcan XC-72 at different rotation speeds are shown in Fig. 14. As can be seen, the average value for the slope of $E - \log[(j_L - j)/j_L]$ plots assuming the reversible oxidation is 28 mV dec^{-1}, independent of rotation rate, whereas a mean value of 22 mV dec^{-1} is found for the $E - \log[j/(j_L - j)]$ plots assuming the irreversible process. Since the slope for the reversible process is very close to its theoretical value of 29.6 mV dec^{-1}, but the slope for the irreversible process is very far from its theoretical value of 59.2 mV dec^{-1}, the reversible HOR has to be considered as the true kinetics.

Because of the absence of a well-defined Tafel region, the exchange current density (j_o) can not be obtained by extrapolating
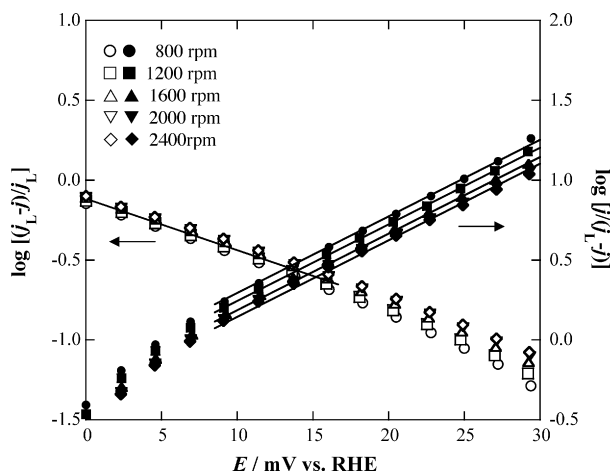
Fig. 14. Tafel slopes assuming reversible (empty symbols) or irreversible (filled symbols) HOR at different RDE rotation speeds under similar conditions to Fig. 12.

the Tafel line, However, it can be estimated from the slope of the linear polarization region near the reversible potential, after correcting for diffusion, also from the hydrodynamic curves of Fig. 12, according to the following equation [8]:

$$\frac{\Delta E}{\Delta j} = \left(\frac{RT}{nF}\right)\left(\frac{1}{j_o} + \frac{1}{j_L}\right) \tag{13}$$

Eq. (13) assumes that the HOR and the hydrogen evolution reaction (HER) follow the same mechanism around the equilibrium potential. After determining $\Delta E/\Delta j$ near the reversible potential and correcting j_o with the active surface area of Pt particles, a true mean exchange current density (j_o') for the HOR of 0.27 mA cm$_{Pt}^{-2}$ was obtained. This value is higher than ca. 0.16 mA cm^{-2} reported for Pt/C catalysts synthesized with VulcanXC-72 and cryogel [8] and differs from 0.65, 0.36 and 0.21 mA cm^{-2} found for HOR in acidic solution at Pt (1 1 0), Pt (1 0 0) and Pt (1 1 1) single crystals, respectively [40,41], also using the RDE technique. Note that the value of 0.27 mA cm^{-2} obtained in the present work is intermediate between those reported for Pt (1 0 0) and Pt (1 1 1), in agreement with the dominant Pt sites of the cubo-octahedral particles here studied.

4. Conclusions

Platinum supported on carbon Vulcan XC-72 and unsupported Pt tested in this paper by XRD have different particle size of 2.6 ± 0.3 and 5.4 ± 0.8 nm respectively, indicating a significant effect of the carbon Vulcan on the dispersion of the nanoparticles. XRD analyses showed the purity and crystallinity of the Pt catalyst nanoparticles. From the mean particle size and within the spherical approximation, a surface area for the supported catalyst of about 108 m^2 g^{-1} is obtained. The HRTEM studies confirmed the crystallinity, purity and particle size of the catalyst. The size-shape plots of the Pt nanoparticles of the carbon-supported catalyst obtained by TEM analyses agree with a dominant cubo-octahedral morphology.

This work has also demonstrated that the amount of ionomer affects the ECSA and the kinetics of the Pt/C-Nafion electrode. The maximum ECSA is found for an optimal composition of the catalyst ink of about 30 wt.% Nafion. The ECSA value for the supported Pt obtained by CO stripping is as high as 73 m^2 g^{-1}. The electrode potential range for CO stripping is in agreement with the cubo-octahedral structure of the nanoparticles, since it mainly corresponds to Pt (1 0 0) and Pt (1 1 1) terrace sites. Although there is no significant peak current in the potential region corresponding to hydrogen adsorption/desorption at the Pt (1 1 1) sites, the ECSA value obtained in this form agrees with CO stripping.

An exponential rise of the inverse Levich intercept with respect to the inverse of the Nafion content is found, with kinetic current densities approaching 15 mA cm^{-2} when the Nafion content in the thin film catalyst layer is smaller than 20 wt.%. HOR for the tested Pt/C catalyst appears to be electrochemically reversible and the estimated exchange current density for the reversible hydrogen reaction is 0.27 mA cm^{-2}$_{Pt}$. All these results indicate that it is an interesting material to be used as a reference in the development of PEMFC catalysts.

References

[1] G. Faubert, R. Cote, D. Guay, J.P. Dodelet, G. Denes, C. Poleunis, P. Bertrand, Electrochim. Acta 43 (1998) 1969.
[2] W. Vielstich, H.A. Gasteiger, A. Lamm, Handbook of Fuel Cells–Fundamentals, Technology and Applications, vol. 3, John Wiley and Sons, Ltd., 2003, pp. 467–472 (Chapter 37).
[3] J.C. Serrano-Ruiz, A. López-Cudero, J. Solla-Gullón, A. Sepúlveda-Escribano, A. Aldaz, F. Rodríguez-Reinoso, J. Catal. 253 (2008) 159.
[4] L. Dos Santos, F. Colmati, E.R. Gonzalez, J. Power Sources 159 (2006) 869.
[5] M. Watanabe, H. Igarashi, K. Yosioka, Electrochim. Acta 40 (1995) 329.
[6] T.J. Schmidt, H.A. Gasteiger, R.J. Behm, J. Electrochem. Soc. 146 (1999) 1296.
[7] T.J. Schmidt, H.A. Gasteiger, G.D. Stäb, P.M. Urban, D.M. Kolb, R.J. Behm, J. Electrochem. Soc. 145 (1998) 2354.
[8] B.M. Babić, L.M. Vračar, V. Radmilović, N.V. Krstajić, Electrochim. Acta 51 (2006) 3820.
[9] L. Calvillo, M.J. Lázaro, E. García-Bordejé, R. Moliner, P.L. Cabot, I. Esparbé, E. Pastor, J.J. Quintana, J. Power Sources 169 (2007) 59.
[10] Y. Xiong, J.M. McLellan, J. Chen, Y. Yin, Z.Y. Li, Y. Xia, J. Am. Chem. Soc. 127 (2005) 17118.
[11] P.N. Ross, Electrochim. Acta 36 (1991) 2053.
[12] Y. Tan, X. Dai, Y. Li, D. Zhua, J. Mater. Chem. 13 (2003) 1069.
[13] A. Miyazaki, S. Yoshida, Y. Nakano, I. Balinty, Chem. Lett. 34 (2005) 74.
[14] R. Narayanan, M.A. El-Sayed, Nano Lett. 4 (2004) 1343.
[15] S. Kinge, C. Urgeghe, A. De Battisti, H. Bönnemann, Appl. Organometal. Chem. 22 (2008) 49.
[16] T.J. Schmidt, M. Noeske, H.A. Gasteiger, R.J. Behm, P. Britz, H. Bönnemann, J. Electrochem. Soc. 145 (1998) 925.
[17] R.B. Lin, S.M. Shih, J. Solid State Electrochem. 10 (2006) 243.
[18] E. Antolini, L. Giorgi, A. Pozio, E. Passalacqua, J. Power Sources 77 (1999) 136.
[19] P. Gode, F. Jaouen, G. Lindbergh, A. Lundblad, G. Sundholm, Electrochim. Acta 48 (2003) 4175.
[20] E. Passalacqua, F. Lufrano, G. Squadrito, A. Patti, L. Giorgi, Electrochim. Acta 46 (2001) 799.
[21] M. Uchida, Y. Fukuoka, Y. Sugawara, N. Eda, A. Ohta, J. Electrochem. Soc. 143 (1996) 2245.
[22] G.C. Li, P.G. Pickup, J. Electrochem. Soc. 150 (2003) C745.
[23] Z. Qi, A. Kaufman, J. Power Sources 113 (2003) 37.
[24] J. Maruyama, I. Abe, Electrochim. Acta 48 (2003) 1443.
[25] Z. Liu, X.Y. Ling, X. Su, J.Y. Lee, J. Phys. Chem. B 108 (2004) 8234.
[26] Z. Hou, B. Yi, H. Yu, Z. Lin, H. Zhang, J. Power Sources 123 (2003) 116.
[27] M.B. Kerber, E. Schafler, M.J. Zehetbauer, Rev. Adv. Mater. Sci. 10 (2005) 427.
[28] H.E. Swanson, E. Tatge, Natl. Bureau Standards Circular (USA) 1 (1953) 95.
[29] X. Wei, H. Sheng, W. Tian, Int. J. Heat Mass Transfer 49 (2006) 3338.
[30] J.R.C. Salgado, J.J. Quintana, L. Calvillo, M.J. Lázaro, P.L. Cabot, I. Esparbé, E. Pastor, Phys. Chem. Chem. Phys. (2008), doi:10.1039/b809227c.
[31] E. Herrero, J. Mostany, J.M. Feliu, J. Lipkowski, J. Electroanal. Chem. 534 (2002) 79.
[32] N.M. Markovic, H.A. Gasteiger, P.N. Ross, J. Phys. Chem. 99 (1995) 3411.
[33] A. Sarapuua, A. Kasikovb, T. Laaksonenc, K. Kontturic, K. Tammeveskia, Electrochim. Acta 53 (2008) 5873.
[34] Z. Chen, L. Xu, W. Li, M. Waje, Y. Yan, Nanotechnology 17 (2006) 5254.
[35] G. Sasikumara, J.W. Ihma, H. Ryua, Electrochim. Acta 50 (2004) 601.
[36] T. Ioroi, N. Fujiwara, Z. Siroma, K. Yasuda, Y. Miyazaki, Electrochem. Commun. 4 (2002) 442.
[37] P.L. Cabot, E. Guezala, J.C. Calpe, M.T. García, J. Casado, J. Electrochem. Soc. 147 (2000) 43.
[38] Y.H. Shih, G.V. Sagar, S.D. Lin, J. Phys. Chem. C 112 (2008) 123.
[39] A.J. Bard, L. Faulkner, Electrochemical Methods. Fundamentals and Applications, John Wiley & Sons, New York, 1981 (Chapter 8).
[40] N.M. Markovic, B.N. Grgur, P.N. Ross, J. Phys. Chem. B 101 (1997) 5405.
[41] T.J. Schmidt, P.N. Ross, N.M. Markovic, J. Electroanal. Chem. 524–525 (2002) 252.